Determination of winter precipitation types

(Schuur, T., and H. Reeves)

1. Introduction

Parallel to the observational efforts, work has continued to develop an improved hydrometeor classification algorithm that combines polarimetric radar observations with thermodynamic information from numerical models. In addition to providing more information to aid in the interpretation of polarimetric signatures, the thermodynamic information provides a mechanism to produce surface-based classification results at distant ranges from the radar, where low-level layers of warm/cold air that fall well below the lowest available radar data might result in microphysical processes that would otherwise remain undiagnosed. The benefit of adding the thermodynamic data is therefore twofold: 1) to enhance classification capabilities in regions where polarimetric radar data are available, and 2) to extend classification capabilities to regions where it is not (Schuur et al. 2011). The project also seeks to provide an algorithm framework that allows ongoing observational work, as listed above, to be easily incorporated into future algorithm development with the long term goals of improving automated precipitation type classification at both the surface and aloft, including the capability to remotely diagnose conditions favorable for liquid water generation.

2. Algorithm development

The classification algorithm is similar to that submitted under this task in September of 2010, except that it has been modified to use higher resolution model data that is mapped to a radar-centric coordinate system, thereby providing better resolution and improved diagnostic capabilities. The initial classification is performed using output from the High-Resolution Rapid-Refresh (HRRR) model analyses, which are created by interpolating the 13-km grid-spaced Rapid-Refresh analyses to a 3.1-km spacing using a 16-point bi-linear interpolation method. The analyses are produced every hour by assimilating observed variables into the 1-hr forecast from the previous cycle using a variational three-dimensional analysis scheme. Vertical profiles of the wet-bulb temperature T_W are calculated across the model grid using T, T_d, and p. If the surface wet-bulb temperature $T_{Ws} \geq 3°C$, it is assumed that precipitation at the surface is rain. However, if $T_{Ws} < 3°C$, the vertical profile of T_W at that point is classified as belonging to one of the four different types shown in Fig. 1. H_0, H_1, and H_2 in Fig. 1 depict the heights of the 0°C crossing points in the profiles. Making use of the studies by Czys et al. (1996), Zerr (1997), and Rauber et al. (2001), the T_W profiles are then used to create a background classification (see flow chart presented in Fig. 2) that consists of six precipitation categories. In this procedure, the threshold for the maximum and minimum acceptable T_W profiles in the warm (T_{Wmax}) and cold (T_{Wmin}) layers, respectively, are derived from a visual inspection of the scatterplots presented by Figs. 5 and 6 of Zerr (1997). Finally, following the procedures outlined in Table 1, polarimetric radar data are used to fine tune the initial classification by determining whether or not it is consistent with the radar observations. For example, a polarimetric radar observation of a bright

band would be inconsistent with a model-based surface classification of dry snow. Radar data are also used to refine a precipitation type within a category, such as by using Z and Z_{DR} observations to discern between ice crystals and dry snow. The algorithm outputs 9 classes of hydrometeors: crystals (CR), dry snow (DS), wet snow (WS), ice pellets/sleet (IP), freezing rain (FR), a mix of freezing rain and ice pellets (FR/IP), rain (RA), heavy rain (HR), and hail (HA).

In the past year, the algorithm submitted with the September 2010 report has been modified in the following ways:

- Reconstructed RHIs are now created using model output that is written to a cylindrical coordinate system. This improves upon the previous version of the algorithm, which wrote the model output to a virtual volume. This means that reconstructed RHIs of model output (as overlaid on the radar data) no longer have a "cone of silence" at close ranges to the radar and have a much finer vertical resolution at more distant ranges from the radar.

- Plotting functions have been improved to help diagnose algorithm performance. In particular, three color bars have been added below each of the reconstructed RHI plots to allow a gate-by-gate evaluation of the 1) vertical profile type, 2) background precipitation type, and 3) radar modified precipitation type.

- Flags have been added to the main program to more easily choose data types and processing and plotting options. It also allows large sections of code to be easily commented out for testing purposes.

- A new program has been written to extract a vertical sounding of T_W for any given radar gate. These profiles can be compared with the conceptual profiles shown in Fig. 1 to analyze algorithm performance.

- The flow chart (Fig. 2) and table showing parameters for radar modification of the background classification (Table 1) have been updated to make them more consistent with the code and textual description of the algorithm.

- Fixed an error to assure that each elevation angle is being checked for a bright band signature.

- Fixed an error in determining median bright band height to allow more wet snow to reach the surface.

- Reorganized code and improved commenting.

An updated list of IDL routines is listed in the Appendix. In addition to improving the algorithms data resolution and diagnostic capabilities, these changes should also make it easier to test new concepts as part of future algorithm development.

3. Case study examples

In late spring of 2009, the NOAA/NWS/Radar Operations Center and its contractor (L3 Baron) took over operational control of the KOUN WSR-88D radar for the purpose of developing the engineering design that would serve as the prototype for the future upgrade of the entire WSR-88D network. Over much of the following 2 years, either no polarimetric data or polarimetric data of questionable quality were collected by KOUN as the contractor worked to improve automated calibration procedures. As a result, our work over the past 2 years has relied heavily upon polarimetric data collected by the C-band OU-PRIME radar. In this section, we examine algorithm output for 3 winter storm events sampled by the OU-PRIME radar on 24 December 2009, 28 January 2010, and 1 February 2011. In total, 31 volumes of radar data (corresponding to 31 hourly HRRR grids) were processed for these 3 events. Reconstructed RHIs of polarimetric variables with HRRR T_W fields overlaid were then produced for every 5° of azimuth. Here we show classification results and reconstructed RHIs for each of the 3 winter events to illustrate current algorithm analysis and classification capabilities. In particular, we focus on some of the precipitation features that are discussed in the observational analysis.

a. 24 December 2009

On 24 December 2009, central Oklahoma experienced a historic winter storm that has become widely known throughout Oklahoma as the "Christmas Eve Blizzard". As the storm system moved into Oklahoma from the southwest in the early morning hours of 24 December 2009, many locations in central Oklahoma began to experience light freezing rain. By mid to late morning, the light freezing rain had transitioned to sleet and light snow and, by mid afternoon, heavy snow with wind gusts exceeding 60 mph (27 m s^{-1}) was common over much central Oklahoma, leading the Norman office of the National Weather Service to issue a Blizzard Warning – a rare occurrence for the southern Great Plains.

Fig. 3 shows 0.5° elevation OU-PRIME data and algorithm classification results at the surface for 170019 UTC on 24 December 2009. At this time, sleet and light snow driven by winds gusting to 40 mph (18 m s^{-1}) was falling over much of central Oklahoma. Further towards the southeast, the radar data show relatively light reflectivities of $Z < 20$ dBZ over a broad region where $Z_{DR} > 2$ dB. This region seems to be consistent with the newly discovered (and yet unpublished, but discussed extensively in previously submitted quarterly reports) low-level Z_{DR} signature that appears to be related to the refreezing of melted or partially melted drops. The background vertical profile type (type 4, see Fig. 3d) and precipitation type (FR/IP and IP categories, see Fig. 3e) also both indicate that this broad region had conditions favorable towards the generation of ice pellets and/or a ice pellet/freezing rain mix. It should also be noted that the algorithm output also indicates that the region of ice pellets had a "branch" that extended well to the west of the OKC metro area. The radar modification of the background classification, as shown by Fig. 3f, indicates that small pockets of low ρ_{HV} at the western periphery of this ice pellet region were reclassified to be wet snow. Future work will need to include more

focused efforts to collect information on precipitation type in an attempt to better validate these types of features in the algorithm output.

The low-level increase in Z_{DR} is further illustrated by Figs. 4 and 5, which show reconstructed RHIs at the azimuths of 20° and 205°, respectively. The enhanced Z and Z_{DR} and drop in ρ_{HV} in Figs. 4a-c all provide a clear indication of an elevated warm layer that seems to be consistent in both height and depth with the relatively weak warm layer indicated by the HRRR T_W field (Fig. 4d). The most notable feature in this RHI is the evolution of the Z_{DR} field beneath the radar bright band. At just below 1 km in height, a rather remarkable increase in Z_{DR} (Fig. 4b) is seen to take place within a layer of < -5°C air (Fig. 4d). As drops freeze within this layer, an accompanying drop in Z (Fig. 4a) is also noted to take place (Fig. 4a). This drop in Z is likely due to a change in the dielectric constant as the drops freeze. While we do not yet fully understand the microphysical process that might be responsible for the increase in Z_{DR} in this layer, we have observed it in numerous winter storms, so it appears to be a repeatable feature. The layer of high Z_{DR} can also be observed in Fig. 5 at 205° azimuth for ranges < 20 km from the radar. As in Fig. 4, the low-level increase in Z_{DR} here also appears to be collocated with a low-level layer of < -5°C air. At higher altitudes, the model output (Fig. 5d) indicates that the elevated warm layer narrows and eventually disappears at a range of about 45 km from the radar. While the radar data shown in Fig. 4a-c seemed to be consistent in both height and depth with the model-diagnosed elevated warm layer, the radar data along 205° azimuth show that the high Z_{DR} and low ρ_{HV} bright band signatures drop noticeably in height with range, suggesting that the model-diagnosed elevated warm layer is too high. The disappearance of the elevated warm layer in both the radar data and model output, however, which corresponds in the surface classification with the transition from ice pellets to snow, both occur at ranges of between approximately 35 to 45 km from the radar.

b. 28 January 2010

The second major storm of the 2009-2010 winter season occurred on 28 January 2010. Unlike the Christmas Eve Blizzard, this storm was primarily known as a severe freezing rain event as a large swath of freezing rain with an accumulation > 0.25 inch (6.4 mm) extended from southwest to northeast Oklahoma. In particular, a broad region in southwest Oklahoma received > 0.75 inch (19.1 mm) of freezing rain with some locations receiving an accumulation of between 1.0 and 1.5 inches (25.4 - 38.1 mm), causing widespread damage. Here we compare the combined polarimetric radar data and model output for this storm to that of the very different Christmas Eve Blizzard, which was primarily a heavy sleet and snow event.

Fig. 6 shows 0.5° elevation OU-PRIME data and algorithm classification results at the surface for 130011 UTC on 28 January 2010. At this time, heavy freezing rain was falling over much of southwest Oklahoma. Because there are no distinguishable differences in polarimetric radar data between rain and freezing rain, radar data alone can not be used to diagnose where one might expect a transition from rain to freezing rain to take place. The vertical profile type (type 4, see Fig. 6d) over the central one-third of the

analysis domain is consistent with either ice pellets or freezing rain. The T_{Wmax} and T_{Wmin} parameters specified in the background classification scheme, however, correctly assigned the background precipitation type (Fig. 6e) to be freezing rain. We do not know whether the thin line of FR/IP on the northern fringe of the area of FR was consistent with observations or not. Because this was primarily a freezing rain event at this time, and also because radar data alone can not be used to distinguish between rain and freezing rain, very few modifications were made to the background classification by the addition of radar data (Fig. 6f). Two exceptions are the result of an addition to the code that resulted in several heavy rain classifications when $35 < Z < 55$ dBZ and a few erroneous reclassifications of WS at ranges of between approximately 70-100 km from the radar, which are likely due to beam broadening effects of a very intense bright band signature. This is something that will have to be examined in more detail with future algorithm development efforts.

Fig. 7 shows a reconstructed RHI through Fig. 6 at 255° azimuth. When compared to the RHIs shown in Figs. 4 and 5 for the 24 December 2009 winter storm, it can be seen that the melting level for each of the storms are at comparable heights, but that the depth and intensity of the warm layer for the 28 January 2010 event was much greater. Combined with the slightly shallower and warmer near-surface layer of cold air, it can be easily seen why the background classification for the 24 December 2009 event was correctly assigned to the ice pellet category while the background classification for the 28 January 2010 event was correctly assigned to the freezing rain category. This suggests that our T_{Wmax} and T_{Wmin} parameters, while possibly needing some fine tuning in the future, are close to being on target. The most notable feature when examining the radar data (Figs. 7a-c) in the RHI is the intense bright band signature, which tends to verify both the intensity and height of the elevated warm layer at ranges close to the radar. The radar data do suggest a very slight drop in the height of the elevated warm layer at greater distances from the radar though, as noted earlier, this may have been largely due to beam broadening.

c. 1 February 2011

The final winter storm system that we examined as part of this years task is the event of 1 February 2011. This event had some similarities to the Christmas Eve Blizzard of 24 December 2009 in that it exhibited periods of light freezing rain, heavy sleet, and snow with winds that occasionally exceeded 40 mph (18 m s^{-1}). Fig. 8 shows 0.5° elevation OU-PRIME data and algorithm classification results at the surface for 060403 UTC on 1 February 2011. Over the 3 hour period prior to this time, reports in OKC indicated that the precipitation type had transitioned from light freezing rain to sleet that was sometimes accompanied by thunder.

At approximately 0600 UTC, the first reports of snow were recorded in the OKC metro area. At this time, Fig. 8 shows that most of the precipitation had moved off to the east of central Oklahoma. Though Z in this region was generally much higher than that observed in the 24 December 2009 event, an extensive region with $Z_{DR} > 2$ (Fig. 8b) that was similar to that seen in the 24 December 2009 event was also observed over a broad

area that had a background precipitation type of FR/IP (Fig. 8e). In this case, however, it appears that much of this high Z_{DR} signature might be attributable to a "downward excursion" of the radar bright band, resulting in a wet snow signature at the surface (see area of WS classified in Fig. 8f). The origins of this region can be better understood by examining Fig. 9, which shows a reconstructed RHI through Fig. 8 at 85° azimuth. A comparison of radar Z, Z_{DR}, and ρ_{HV} bright band signatures with the HRRR T_W fields along several RHIs and over a several hour period (not shown) suggests that the model-diagnosed elevated warm layer was too high and too intense for this event. This can also be seen in Fig. 9, which clearly shows that the top of the radar-observed radar bright band falls well below the top of the model-diagnosed elevated warm layer. This is particularly evident in Fig. 9 at ranges of between 20 and 40 km from the radar, where a noticeable dip in the bright band signature suggests that heavy wet snow is reaching the surface. Such localized regions of heavy wet snow are sometime hard to forecast and are likely the product of feedback between microphysics and thermodynamics, such as localized cooling due to enhance melting and evaporation.

4. Conclusions and future development

Observational analyses have revealed several repeatable polarimetric signatures in winter weather events that appear to provide information on microphysical processes such as the refreezing of water drops in a low-level cold layer, downward excursions of the radar bright band, and elevated layers of high Z_{DR} and K_{DP} that appear to be related to dendritic growth. Concurrent with the observational analyses, work has continued to improve automated techniques of combining polarimetric radar data with thermodynamic output from numerical models to improve classification of precipitation type in winter storms. Several changes have been made in the algorithm over the past year in order to retain a higher vertical resolution of the model output, enhance the algorithm design to make it easier to test future concepts, and improve algorithm diagnostic capabilities. The algorithm was tested on a total of 31 volumes of radar data on 3 winter storm events that were sampled by the OU-PRIME radar. Overall, the algorithm appears to demonstrate some skill at classifying precipitation type at the surface. Future work, however, will need to include the collection of more comprehensive ground-based observations for the purpose of validating the algorithm results.

In the coming year, comprehensive analysis of cold-season storms with high icing potential will be continued. The rapidly expanding network of polarimetric WSR-88D radars will provide opportunities to capture cases with documented icing (PIREPs) suitable for analysis of polarimetric radar signatures. NSSL will rely on guidance from Lincoln Laboratory for identification of the high-impact icing events in the radar coverage of the newly deployed polarimetric WSR-88D radars (e.g., in Chicago and Cleveland).

In addition to the wet bulb temperature, which is utilized exclusively in the current winter HCA, the following meteorological fields will also be analyzed. Relative humidity will be explored to detect the areas of supersaturation with respect to ice / water and winds retrieved from the model and radar will be examined to assess possible impact

of advection on polarimetric signatures. The current winter HCA has been designed to identify freezing rain / drizzle associated with melting in an elevated warm layer. Special emphasis will now be given to the "supercooled warm rain process" responsible for generation of supercooled drizzle in absence of the melting layer aloft.

Background classification based on thermodynamic data in the existing winter HCA will be refined using a one-dimensional (1D) model of snow melting / refreezing. Another 1D model describing transition from crystals to snow aggregates and recently developed at NSSL also will be utilized to better understand the role of supercooled liquid water (SLW) in the generation of the "second bright band" signature aloft.

An attempt will be made to incorporate a newly discovered signature of Z_{DR} (differential reflectivity) enhancement due to refreezing of supercooled raindrops in the modified winter HCA. Potential role of using Z_{DR} columns for short-term convective forecasts will be further examined. Maps of integrated Z_{DR} in the columns above the freezing level will be generated together with the maps of surface reflectivity Z (or VIL) as well as cloud height tops. Links between these will be evaluated to assess the value of Z_{DR} columns for localizing convective updrafts and convective development forecasting.

5. References

Czys, R., R. Scott, K. Tang, R. Przybylinski, and M. Sabones, 1996: A physically based nondimensional parameter for discriminating between locations of freezing rain and sleet. *Wea. Forecasting*, **11**, 591-598.

Rauber, R. M., L. S. Olthoff, M. K. Ramamurthy, and K. E. Kunkel, 2001: Further investigations of a physically based, nondimensional parameter for discriminating between locations of freezing rain and ice pellets. *Wea. Forecasting*, **16**, 185-191.

Schuur, T. J., Park, H.- S., A. V. Ryzhkov, and H. Reeves, 2011: Classification of precipitation types during transitional winter weather using the RUC model and polarimetric radar retrievals. *J. Appl. Meteor.*, In review.

Zerr, R. 1997: Freezing rain, an observational and theoretical study. *J. Appl. Meteor.*, **36**, 1647-1661.

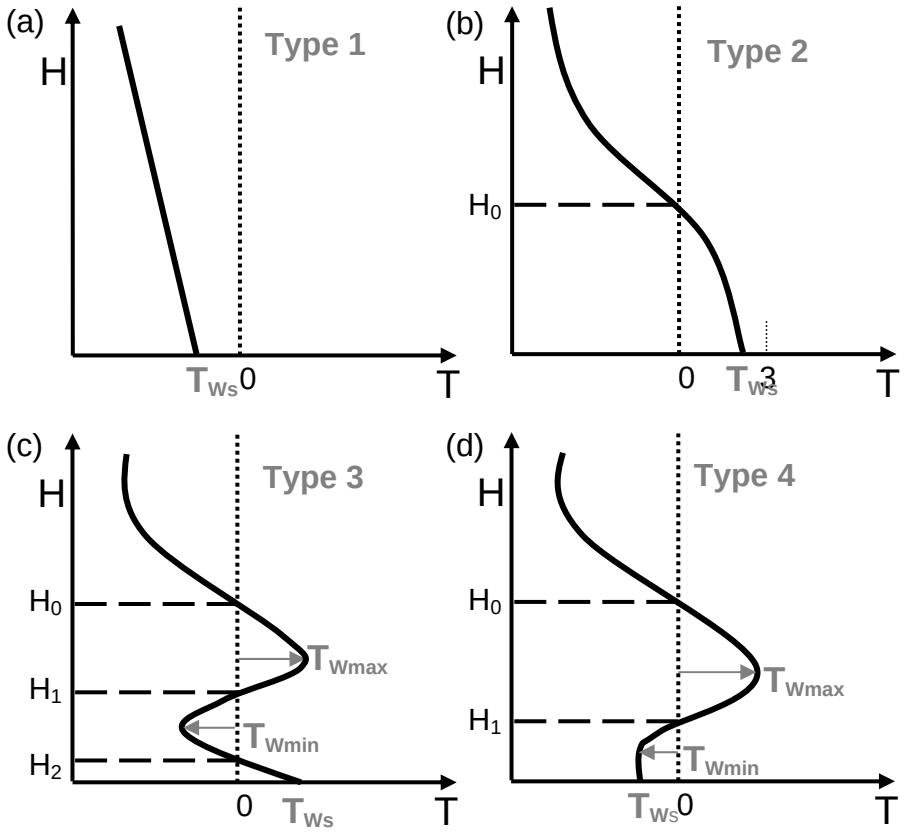

Fig. 1. Four types of vertical profiles of wet-bulb temperature (T_w) corresponding to four or more types of precipitation.

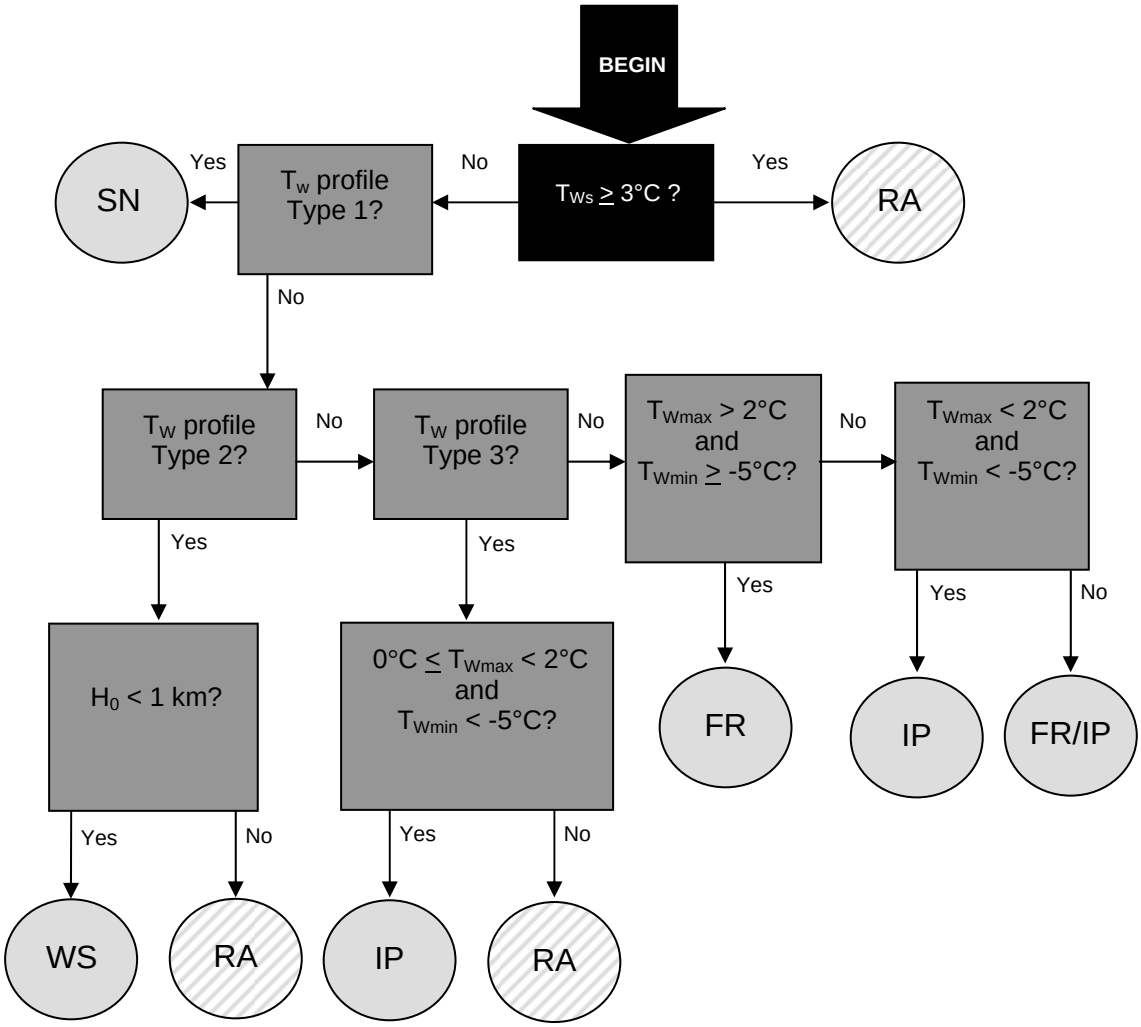

Fig. 2. Flow chart showing logistic for determination of precipitation types depending on vertical profile of wet bulb temperature.

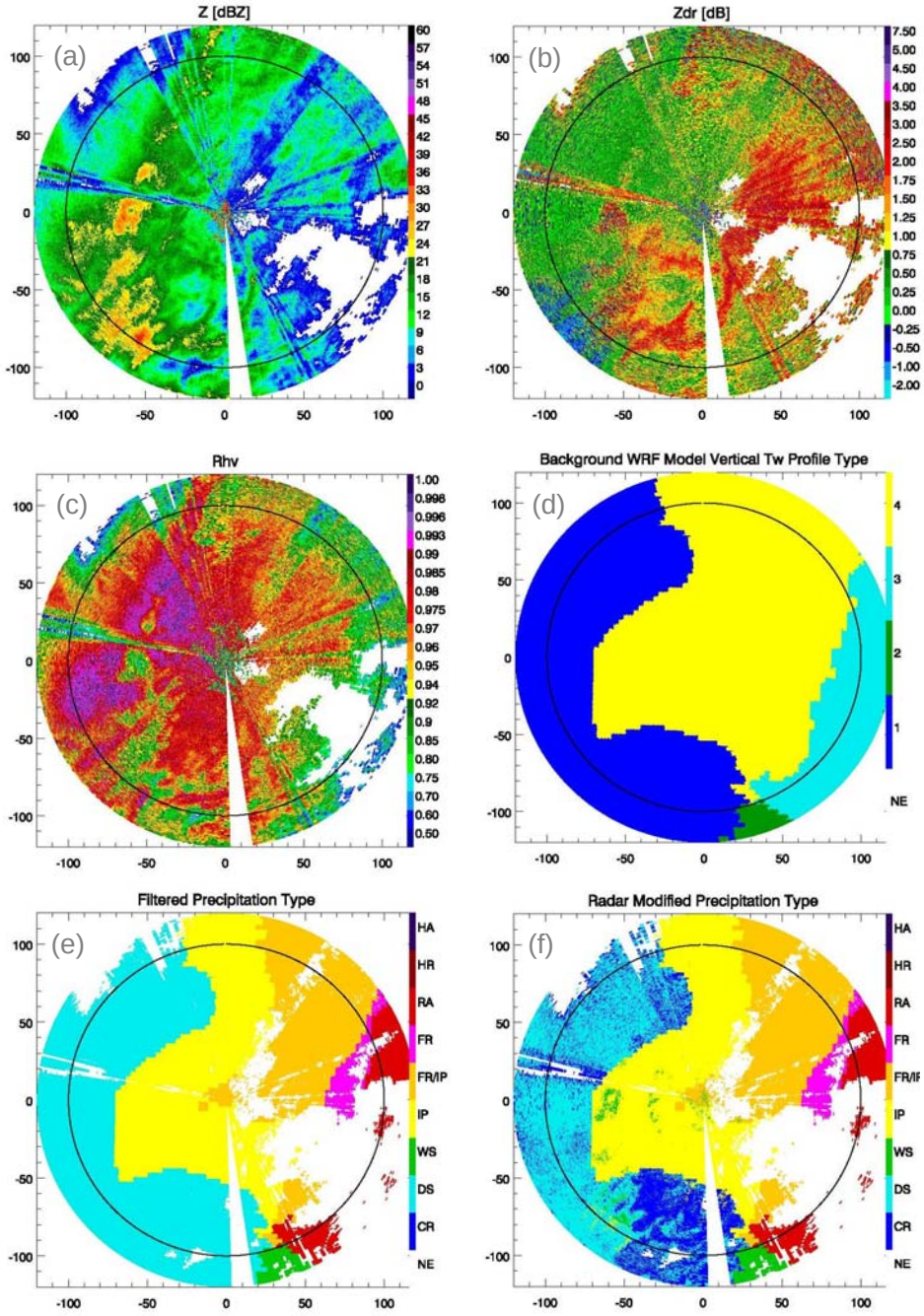

Fig. 3. OU-PRIME PPI radar data at 0.5° elevation angle (a-c) and corresponding algorithm output (d-f) at the surface for 170019 UTC on 24 December 2009. Panels represent (a) radar reflectivity, (b) differential reflectivity, (c) correlation coefficient, (d) vertical profile type, (e) background precipitation type, and (f) radar modified precipitation type. Vertical profile types in panel (d) can be compared to those shown in Fig. 1.

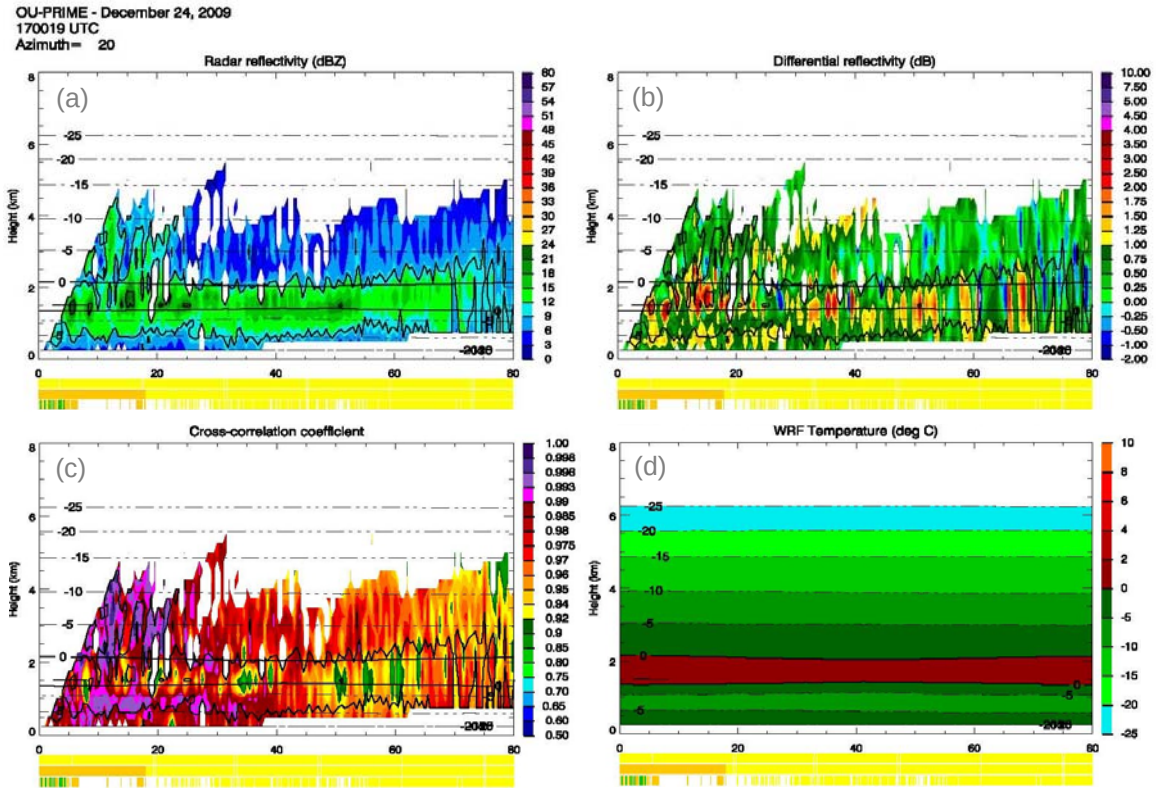

Fig. 4. Reconstructed RHI through panels shown in Fig. 3 at 20° azimuth. Panels represent (a) radar reflectivity, (b) differential reflectivity, (c) correlation coefficient, and (d) T_W from the HRRR model output. T_W profiles are also overlaid on each of the plots. Three color bars at bottom of panels correspond to vertical profile type, background precipitation type, and radar modified precipitation type for each gate (colors corresponding to those in Fig. 3d-f), respectively.

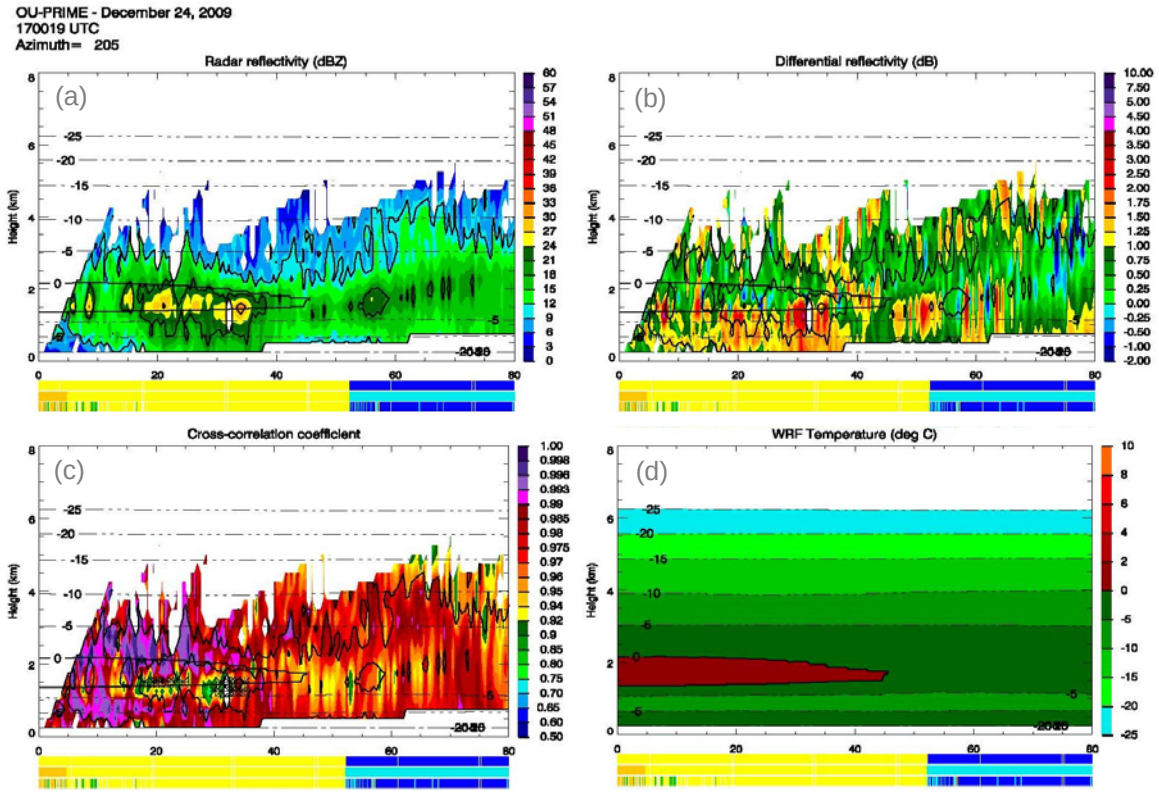

Fig. 5. Reconstructed RHIs through panels shown in Fig. 3 at 205° azimuth. Panels represent (a) radar reflectivity, (b) differential reflectivity, (c) correlation coefficient, and (d) T_W from the HRRR model output. T_W profiles are also overlaid on each of the plots. Radar bright band detections in panel (c) are indicated by the asterisks. Three color bars at bottom of panels correspond to vertical profile type, background precipitation type, and radar modified precipitation type for each gate (colors corresponding to those in Fig. 3d-f), respectively.

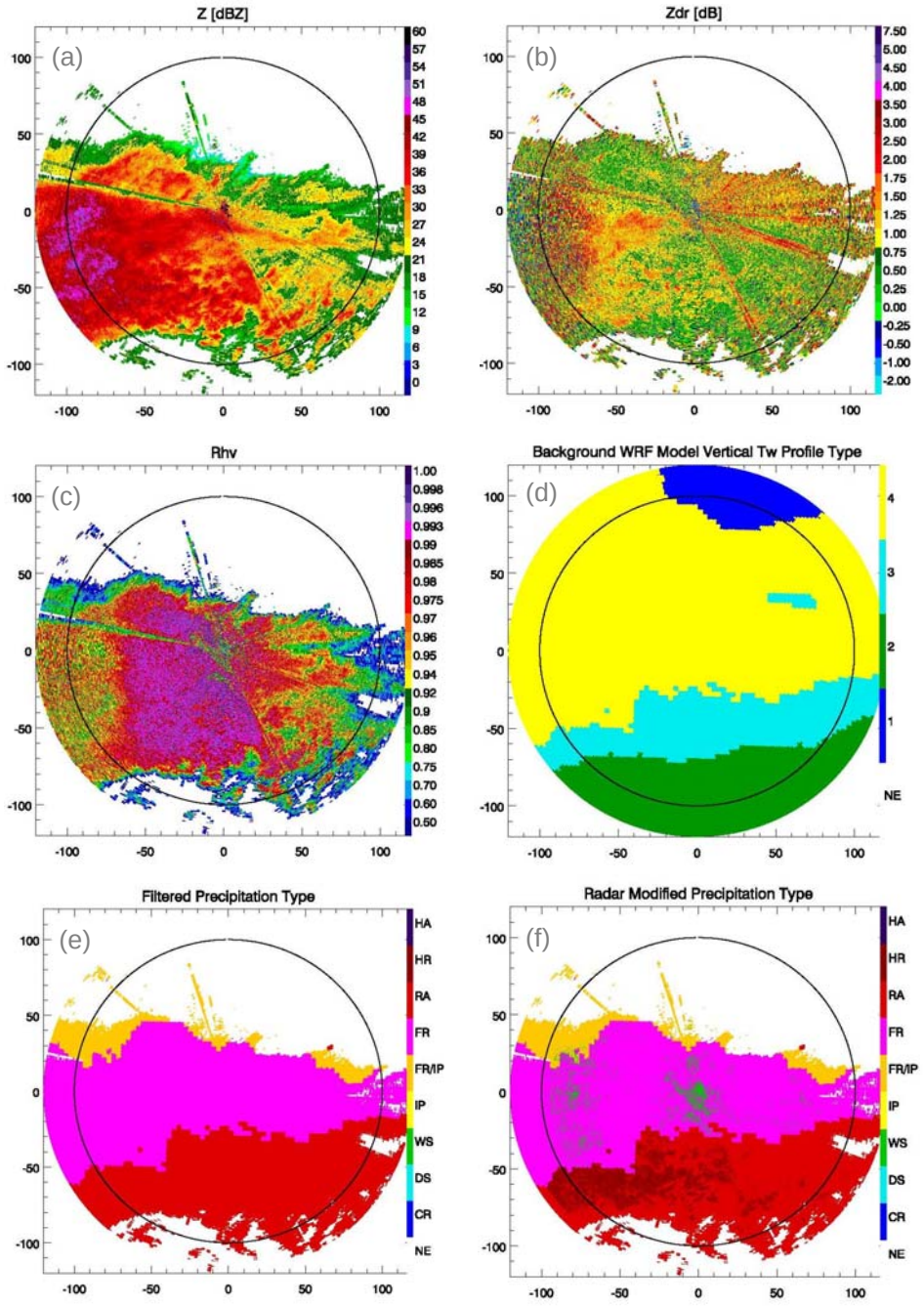

Fig. 6. OU-PRIME PPI radar data at 0.5° elevation angle (a-c) and corresponding algorithm output (d-f) at the surface for 130011 UTC on 28 January 2010. Panels represent (a) radar reflectivity, (b) differential reflectivity, (c) correlation coefficient, (d) vertical profile type, (e) background precipitation type, and (f) radar modified precipitation type. Vertical profile types in panel (d) can be compared to those shown in Fig. 1.

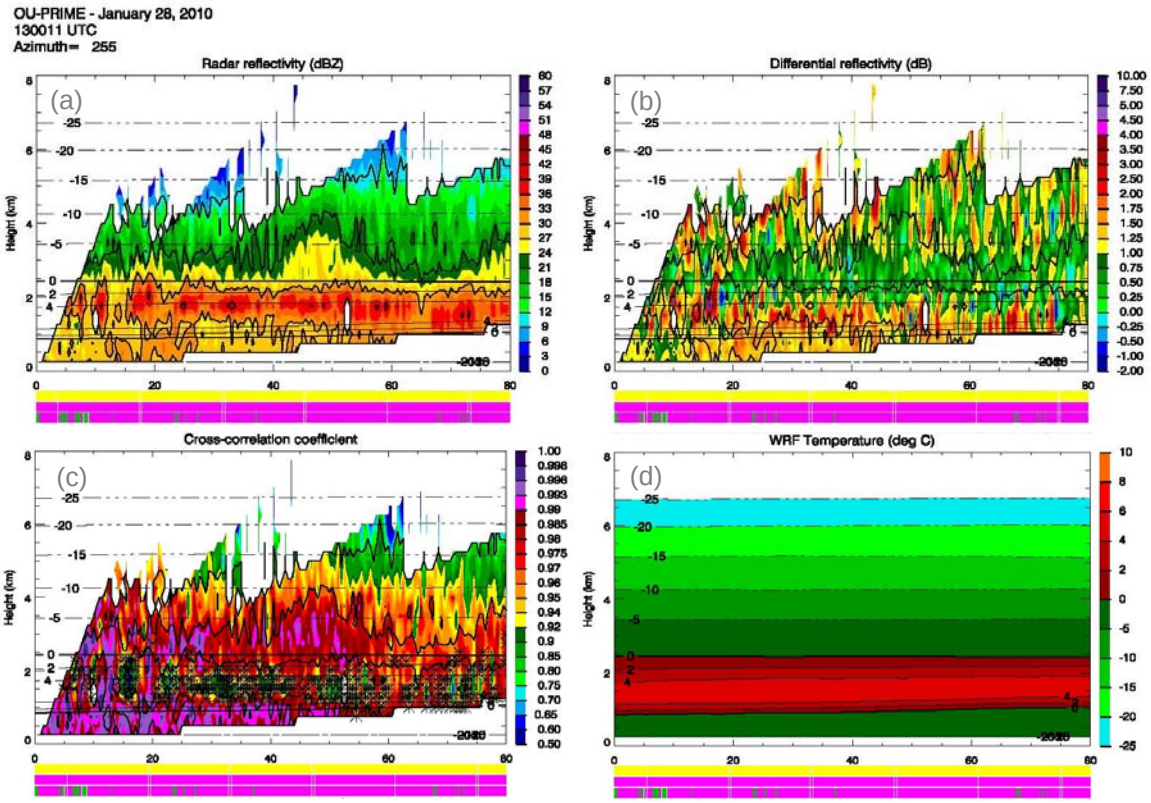

Fig. 7. Reconstructed RHIs through panels shown in Fig. 6 at 255° azimuth. Panels represent (a) radar reflectivity, (b) differential reflectivity, (c) correlation coefficient, and (d) T_W from the HRRR model output. T_W profiles are also overlaid on each of the plots. Radar bright band detections in panel (c) are indicated by the asterisks. Three color bars at bottom of panels correspond to vertical profile type, background precipitation type, and radar modified precipitation type for each gate (colors corresponding to those in Fig. 6d-f), respectively.

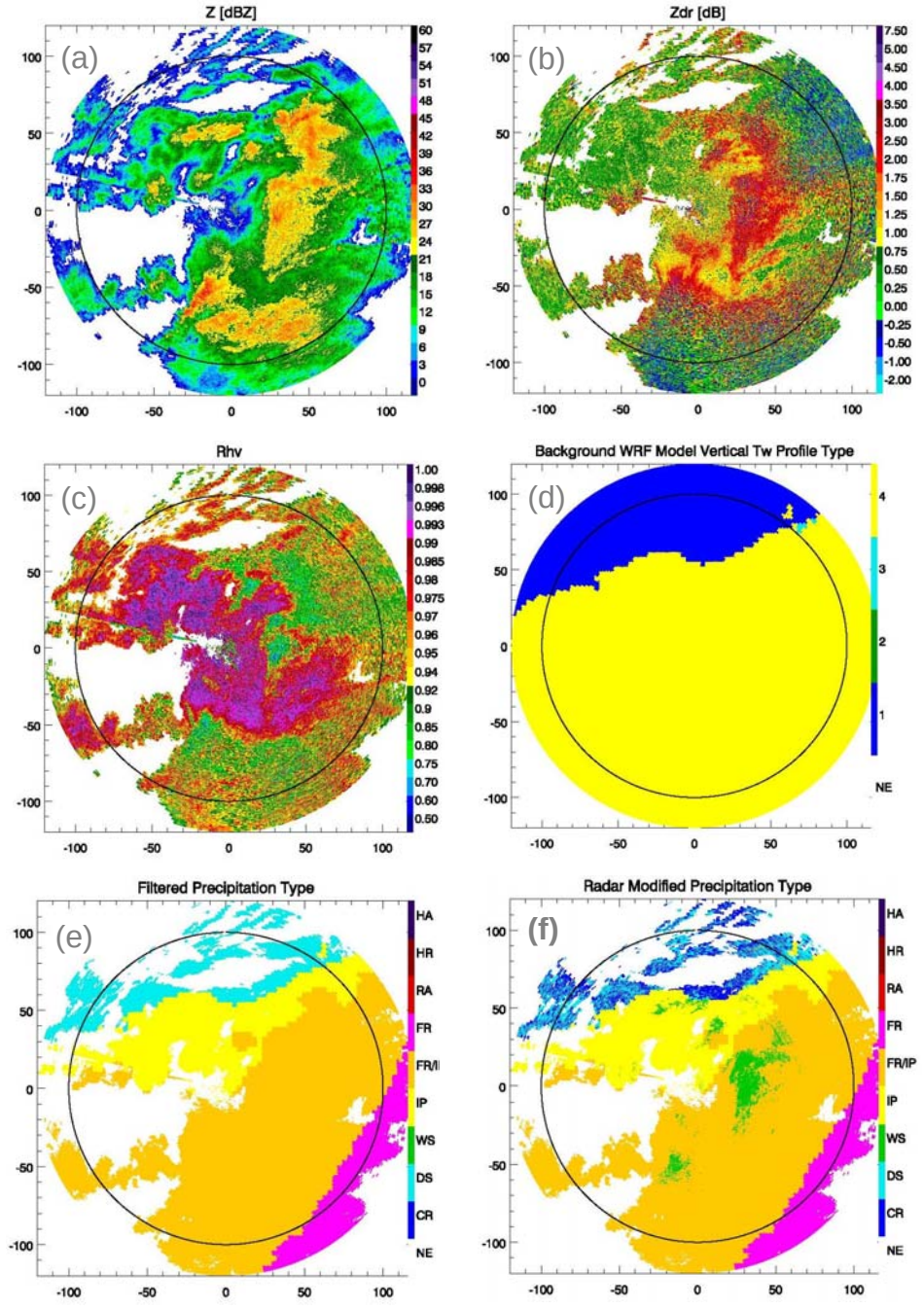

Fig. 8. OU-PRIME PPI radar data at 0.5° elevation angle (a-c) and corresponding algorithm output (d-f) at the surface for 060403 UTC on 1 February 2010. Panels represent (a) radar reflectivity, (b) differential reflectivity, (c) correlation coefficient, (d) vertical profile type, (e) background precipitation type, and (f) radar modified precipitation type. Vertical profile types in panel (d) can be compared to those shown in Fig. 1.

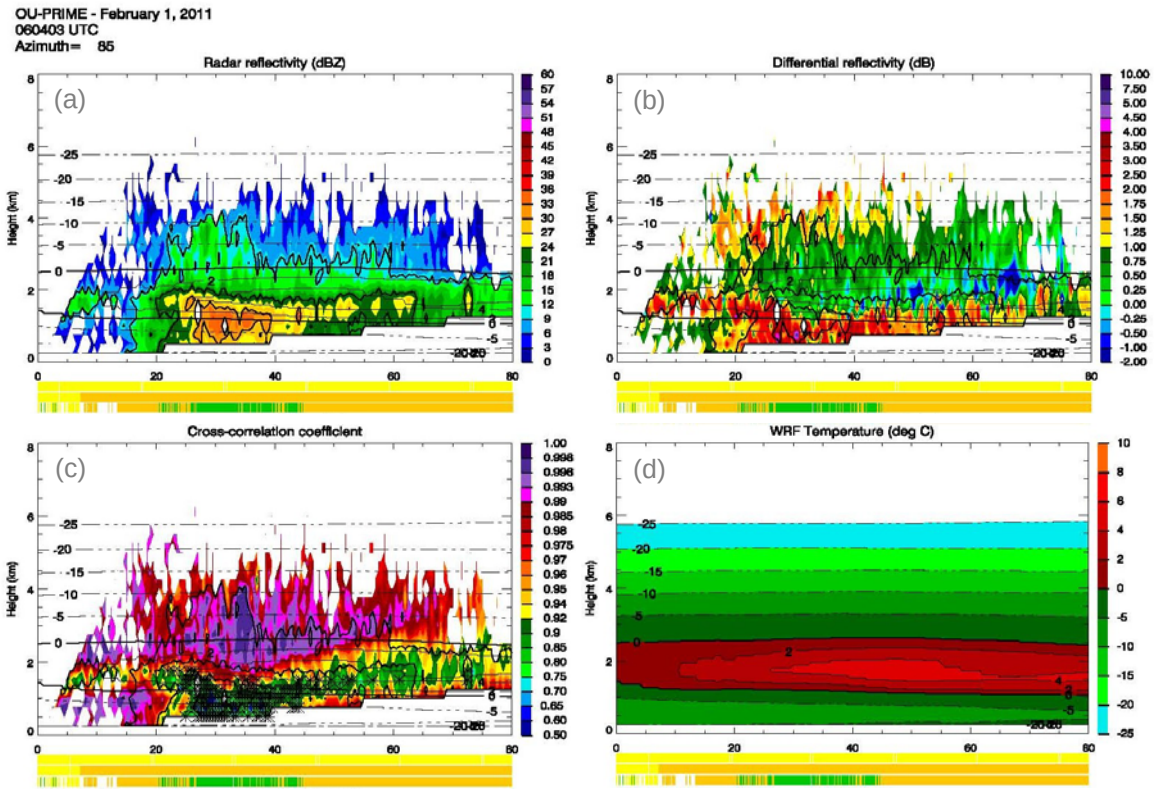

Fig. 9. Reconstructed RHIs through panels shown in Fig. 8 at 85° azimuth. Panels represent (a) radar reflectivity, (b) differential reflectivity, (c) correlation coefficient, and (d) T_W from the HRRR model output. T_W profiles are also overlaid on each of the plots. Radar bright band detections in panel (c) are indicated by the asterisks. Three color bars at bottom of panels correspond to vertical profile type, background precipitation type, and radar modified precipitation type for each gate (colors corresponding to those in Fig. 8d-f), respectively.

Table 1**:** Criteria used for the modification of the background classification based on the radar determination of an elevated warm layer/bright band.

Elevated warm layer	Yes	Yes	Yes	Yes	Yes	Yes
Background class	SN		All class except for RA	IP	FR/IP	RA
Condition	T_{Wmin}< -5 ^{o}C	T_{Wmin}>-5 ^{o}C	Median BBH < 1km			
Surface ID (final)	IP	FR/IP	WS	IP	FR/IP	RA

Elevated warm layer	No		No	No	No	No	No
Background class	SN		IP	FR/IP	RA	FR	WS
Condition	Z_{DR}>0.6 and Z<20 dBZ	otherwise					
Surface ID (final)	CR	DS	IP	FR/IP	RA	FR	WS

Appendix

Description of Code

C++ Programs:

clean_convertWRF.cpp: Extracts Rapid Refresh model data to a location centered on the radar site.

IDL Programs:

Main programs:

OUprime_WRF_classify.pro: Main processing program for the OU-PRIME data. Reads the polarimetric OU-PRIME data by calling *ReadWGnc*. Calls *PreProcess_C* to correct the radar data, calls *makeColumn* to create vertical columns of polarimetric data to look for bright band signatures, and calls *LoadVirtualVolume* to put the OU-PRIME data into a 360° Virtual Volume. Reads the WRF data by calling readWRFnc. Calls *compute_vp_info* to extract vertical profiles of temperature, wet bulb potential temperature, vertical profile type, twmax, twmin, H0, H1, H2, InvBotHeight, and InvTopHeight, calls *convertWRFtoRadial* to convert the extracted WRF information to a polar grid, and calls *LoadVirtualVolumeWRF_OUprime* to put the WRF data into a 360° Virtual Volume that corresponds to the OU-PRIME data. Uses the extracted vertical profile types and logic shown in Figs. 1 and 2 to assign initial precipitation type, modifies that type (when necessary) based on radar observations, applies threshold to clean up the data before plotting, and calls *binplot* several times to create plots of a variety of radar, model, and algorithm fields.

Subroutines:

avr.pro: Computes the running average of a data array. Called by *Preprocess_C.*

binplot.pro: Plots radials from radar data one bin at a time so that they actually look like radials. Called by *OUprime_WRF_classify and OUprime_plot_rhi_loop.*

CalculateTextures.pro: Preprocess the data from *readWGnc* for use in the polametric algorithms. Z and Φ_{DP} from are ingested and texture fields of Z and Φ_{DP} are returned.

colormap.pro: Initializes r,g,b colors and provides color scales and legends for the various polarimetric and thermodynamic model output variables. Called by *binplot.*

compute_kdp.pro: Calculates K_{DP} using a smoothed Φ_{DP}. Called by *Preprocess_C.*

computeGN.pro: Computes gate number. Called by *makeColumn.*

computeHeight.pro: Computes gate height. Called by *makeColumn.*

compute_vp_info.pro: Ingests the WRF model output and computes vertical profile type (Fig. A1), 0°C crossing points H0, H1, and H2 (Fig. A1) for the vertical profile types, T_{wmax}, T_{wmin}, a variety of other model parameters used in the classification process.

convertWRFtoRadial.pro: Converts fields extracted from the WRF model grid by *compute_vp_info* into polar coordinates. Called by *OUprime_WRF_classify.*

fdp_OKU.pro: Processes Φ_{DP} from raw data by identifying good data using a ρ_{hv} threshold, smoothing it with a median filter, and interpolating between good data stretches using a linear average filter. Called by *Preprocess_C.*

FileTimeKOUN.pro: Contains several functions necessary for reading file names. Some of the functions (such as *filepath*) are called by *OUprime_WRF_classify.*

fit.pro: Computes the slope of a linear fit. Called by *compute_kdp.*

GetFiles_radar.pro: Pops up a dialog box that allows radar input files to be selected. Returns an array with the names of all of the radar input files selected. Called by *OUprime_WRF_classify.*

GetFile_wrf.pro: Pops up a dialog box that allows wrf input file to be selected. Returns an array with the names of all of the radar input files selected. Called by *OUprime_WRF_classify.*

loadVirtualVolume.pro: Computes the Virtual Volume of the KOUN or OU Prime radar data. Called by *OUprime_WRF_classify.*

loadVirtualVolumeWRF_OUprime.pro: Converts the WRF data into a OU-PRIME-centered Virtual Volume where data points have a one-to-one correspondence with the radar range gates. Called by *OUprime_WRF_classify.* Contained within file *loadVirtualVolumeWRF.pro*

makeColumn.pro: Computes a vertical column from the Virtual Volume of the radar data. Called by *OUprime_WRF_classify.*

preprocess_c.pro: Preprocess the OU-PRIME data. Corrects Z and Z_{DR} for attenuation and differential attenuation, respectively, corrects ρ_{hv} and Z_{DR} for noise, unfolds Φ_{DP}, and computes K_{DP}. Calls fdp_OKU, compute_kdp, and avr. Called by *OUprime_WRF_classify.*

readWGnc.pro: Reads OU-PRIME data. Takes a filename, opens that file and reads all radials of data out of it. Returns arrays of data in the [bins, num_radials] format, as well as an assortment of header information. Called by *OUprime_WRF_classify.*

readWRFnc.pro: Takes a netcdf WRF file that has been cut down to the OU-PRIME area and reads the data into arrays. Called by *OUprime_WRF_classify.*

Plotting Programs:

OUprime_plot_rhi_loop.pro: Constructs a RHI from the Virtual Volumes of OU-PRIME and WRF data and plots fields of OU-PRIME radar reflectivity, differential reflectivity, correlation coefficient, and correlation coefficient with bright band detections (indicated by asterisks) overlaid at a user defined azimuth. T_w contours from the WRF model data are overlaid on each panel. Color bars at bottom of graph show vertical profile type, background precipitation type, and radar modified precipitation type for each gate. Colors on color bars correspond to corresponding PPI and surface based plots produced by *OUprime_WRF_classify.*

plot_wrf_sounds.pro: Plots a vertical sounding of TW from the grid produced by *OUprime_WRF_classify* at a user specified azimuth and range.